GENESIS AND DEVELOPMENT MECHANISMS OF A MESO-B-SCALE VORTICAL DISTURBANCE OVER THE JAPAN SEA IN WINTER: A HIGH-RESOLUTION NUMERICAL SIMULATION

Shunichi Watanabe* and Hiroshi Niino

Atmosphere and Ocean Research Institute, The University of Tokyo, Kashiwa-shi, Chiba, Japan

1. Introduction

When a cold air breaks out over the Japan Sea in winter, different types of meso-scale vortical disturbances (MVDs) are observed. These MVDs have various spatial scales ranging from meso-γ to meso-α-scales (Kawashima and Fujiyoshi 2005; Asai and Miura 1981; Ninomiya et al. 1990; Ninomiya and Hoshino 1990) and have various types of cloud systems such as comma-shaped clouds or spiral-cloud bands. They also occasionally change their spatial scale and cloud pattern during their development (Lee et al. 1998). Such diversity seems to be a consequence of the difference in their development mechanisms.

These MVDs are known to often bring serious disasters such as heavy snowfall (e.g., Miyazawa 1967; Asai 1988) and strong gusts (e.g., Kuroda 1992; Yamagishi et al. 1992) to coastal regions of the Japan Sea. The prediction of MVDs, however, is still difficult because of their small spatial and time scale. It is important to clarify the mechanisms of generation and development of MVDs not only for advancing our understanding of the atmosphere but also for mitigating natural disasters.

Meso-α-scale lows that occur in a polar airmass are sometimes called polar lows. They develop over high-latitude oceans such as North Atlantic, Barents Sea and Weddell Sea. Satellite images show that polar lows are accompanied by comma clouds or spiral-cloud bands (Rasmussen and Turner 2003). A number of studies have been done on the mechanisms of generation and development of polar lows. These studies suggest that baroclinic instability (Reed and Duncan 1987), thermal instabilities such as CISK (Rasmussen 1979) and WISHE (Emanuel and Rotunno 1989) or both (Yanase and Niino 2007) play important roles in their development. Ninomiya (1989) examined polar lows around Japan in the winter of 1986-1987 and showed that they developed in synoptic-scale cyclonic flows, unstable stratification which is associated with surface heat fluxes below a cold vortex at the mid-troposphere, and strong baroclinicity in the low-level.

As for MVDs of smaller horizontal scale over the Japan Sea, a number of observational studies have been performed using data from meteorological radars and satellite images. Similar MVDs are also observed in the vicinity of the Great Lakes (Hjelmfelt 1990; Laird et al. 2001). Using satellite images, Asai (1988) analyzed locations of MVDs' genesis over the Japan Sea in the winter of 1983-1984. He found that MVDs having horizontal scale less than 300 km are concentrated in two regions: One is from the east of Korea Peninsula to San-in and Hokuriku districts of Japan, and the other in the west of the Hokkaido Island (see Fig. 1 for geographical locations). These regions are called Japan Sea Polar Airmass Convergence Zones (JPCZs) by Asai (1988).

**Corresponding author address*: Shun-ichi Watanabe, Dynamic Marine Meteorology Group, Dept. of Physical Oceanography, Atmosphere and Ocean Research Institute, University of Tokyo, Kashiwa-shi, Chiba Japan
E-mail: watanabe-s@aori.u-tokyo.ac.jp

JPCZs are formed between northerly and westerly wind in its northeastern and southwestern side, respectively, so that they are accompanied by significant convergence, cyclonic shear and active cumulus convection.

The importance of barotropic instability of the horizontal shear has been suggested for the generation and development mechanisms of MVDs on JPCZs (Asai and Miura 1981; Nagata 1993; Kawashima and Fujiyoshi 2005). Nagata (1993) used a hydrostatic numerical model, in which cumulus convection is parameterized, to study meso-β-scale vortical disturbances (MBVDs) on the JPCZ in the east of the Korean peninsula. He succeeded in reproducing realistic MBVDs having spiral bands and a cloud-free eye structure, and showed that they developed through barotropic instability based on an energy budget analysis. Using dual-Doppler radar data, Kawashima and Fujiyoshi (2005) analyzed meso-γ-scale vortical disturbances (MGVDs) along a snowband off the west coast of Hokkaido Island. Their energy budget analysis showed that the MGVDs acquired their energy from horizontal shear flow at the low level and a part of the energy was carried upward by the pressure transport term.

On the other hand, some MBVDs have been suggested to develop baroclinically, because significant baroclinicity exists over the Japan Sea due to airmass transformation and JPCZs themselves have frontal features. Based on observational data, Yamagishi et al. (1992) and Ohkubo (1997) showed that MBVDs were accompanied by front-like structures which are the characteristics of extratropical cyclones. Tsuboki and Wakahama (1992) analyzed a quasi-geostrophic linear instability problem for an idealized JPCZ west of the Hokkaido Island and found two unstable modes which correspond to observed MVDs having horizontal scales of 200-300 km and 500-700 km, respectively. Maejima and Iga (2011) performed a linear instability analysis and a numerical experiment for fronts imitating a JPCZ and showed that MBVDs tend to develop through barotropic instability, while meso-α-scale vortical disturbances through baroclinic instability. They also showed that, as the stratification of the atmosphere becomes weaker, baroclinic development becomes dominant.

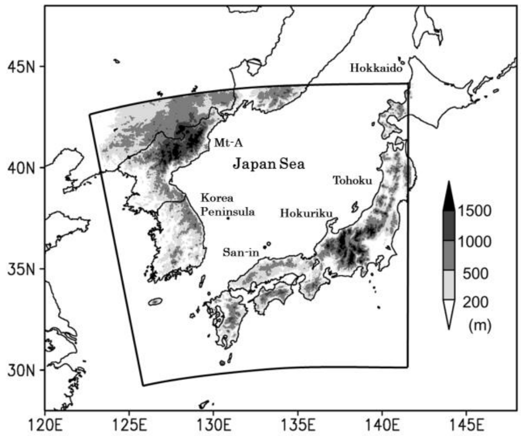

Figure 1. Geographical map of the East Asia. The calculation domain used in the numerical simulation is enclosed by thick black lines.

One of the significant characteristics of the MVDs is their multi-scale structure. Ninomiya et al. (1990) and Ninomiya and Hoshino (1990) investigated MVDs with multi-scale structure, where an MBVD developed in a meso-α-scale low (MAL). While the latter developed in a region with strong baroclinicity, the MBVD developed in a region with strong cyclonic shear and deep convective mixed layer, which were provided by the MAL. Tsuboki and Asai (2004) studied a similar multi-scale structure of a MAL by a numerical simulation using a hydrostatic model. They showed that the MAL was intensified by upper-level divergence of the ageostrophic wind which was formed by updrafts in a baroclinic environment. MBVDs embedded in the MAL developed from horizontal shear flows intensified by the MAL, while they contributed to the development of the MAL by causing strong updrafts.

Since cumulus convection is very active over the Japan Sea in winter, its impact on the development of MBVDs should be examined by a non-hydrostatic model in which cumulus convection is not parameterized. Kato (2005) performed a numerical simulation of an MBVD with non-hydrostatic model having a horizontal resolution of 1 km. His energy budget analysis indicated that the importance of vertical shear production (VSP) associated with strong upward motion of cumulus convection because the horizontal shear of the JPCZ was confined to low level and vertical shear was large above.

As we have reviewed above, the generation and development of MVDs are affected by various phenomena of different scales. Furthermore, MVDs often change their size and cloud pattern through their lifetime. Therefore, it is likely that different mechanisms work at different stages of MVDs' development. One of the powerful tools to study their life cycle may be a high resolution numerical simulation which became possible only recently.

Most of the previous studies on MVDs associated with JPCZs focus on their behavior after a JPCZ is formed. However, MVDs over the Japan Sea are occasionally generated without the presence of a JPCZ (e.g., Fu et al. 2004). On 30 December 2010, an MBVD appeared and developed over the Japan Sea. The JPCZ was not present prior to the development of the MBVD, but was generated as the MBVD developed. In order to study the life cycle of the MBVD from the early stage of its development, when a JPCZ was not formed, to its mature stage, we have performed a high resolution numerical simulation with a non-hydrostatic model and have succeeded in reproducing the observed evolutions of the MBVD and the JPCZ. Here we report the results of the detailed analysis on the structure and development mechanisms of the MBVD. The structure of this paper is as follows. Observational analysis of the MBVD and synoptic situation is made in section 2. In section 3, the numerical model used in the present study is described. Simulation results are presented in section 4 and sensitivity experiments are performed in section 5. A summary is given in section 6.

2. Observational analysis

2.1. Data

The following data provided by Japan Meteorological Agency are utilized in the present study: hourly infrared satellite images of Japanese *Multi-functional Transport Satellite*-2 (MTSAT-2), surface and 500 hPa weather maps, and meso objective analysis (MANAL) data with horizontal resolution of 5 km.

2.2 Evolution of MBVD and JPCZ

Figure 2 shows the MTSAT-2 IR images from 2100 UTC 29 to 0800 UTC 31 December 2010. At 2100 UTC 29, a cloud band extending eastward from 130E, 41N existed (Fig. 2a). It showed a southward bent at 134E, 41N. The southern part of the cloud band was masked by upper-level clouds. No obvious JPCZ was observed at this time. As the cold air outbreak from Siberia intensified, the cloud band marched southward. At 0700 UTC 30, the cloud band extended east-northeastward from 130E, 38.5N (Fig. 2b). Stratiform clouds spread over the northern side of the cloud band and a number of vortices formed along the southern edge of the cloud band. Finally, these vortices merged into an MBVD, which had a horizontal scale of about 150 km and had a cloud-free eye and spiralform clouds, at 135E, 36.5N at 1700 UTC 30 (Fig. 2c). A JPCZ started to form at 0700 UTC 30 from 129E, 40N (Fig. 2b) and extended southeastward to the MBVD (Fig. 2c and 2d). We note that there was also a cloud system with horizontal scale of about 1000 km in the eastern part of the Japan Sea which corresponded to a rapidly deepening meso-α-scale low (Fig. 2c).

According to an analysis by Nakai and Yamaguchi (2012), the MBVD and the JPCZ were accompanied by extremely deep convective clouds which reached the tropopause and brought a record-high snowfall in San-in district (the Japan Sea side of the Chugoku district in the western part of Honshu Island; see Fig. 1).

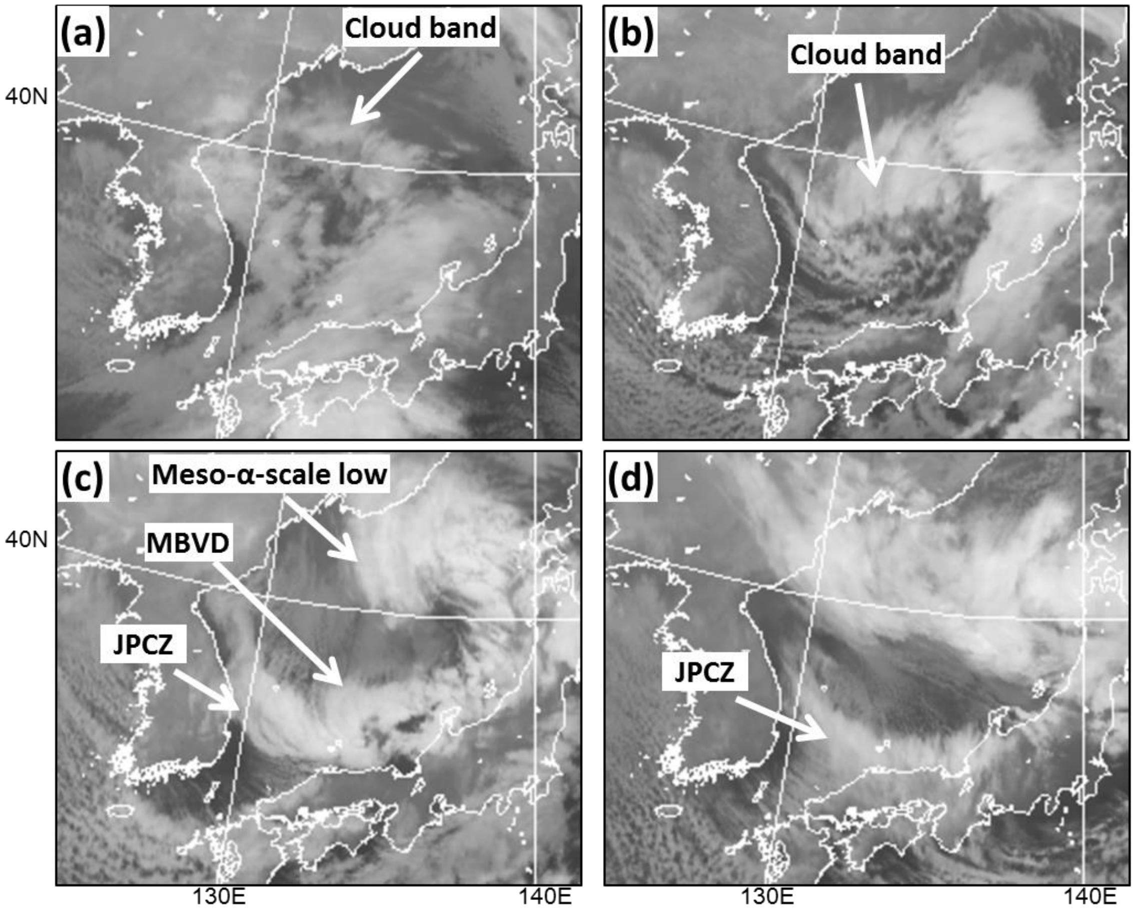

Figure 2. Infrared images of MTSAT-2. (a): 2100 UTC 29 Dec 2010, (b): 0700 UTC 30, (c): 1700 UTC 30, and (d): 0800 UTC 31.

2.3. Synoptic situation

Figures 3 and 4 show weather maps at 500 hPa and surface, respectively, from 1200 UTC 29 to 0000 UTC 31. The synoptic situation in which the MBVD developed was characterized by a cold vortex at 500 hPa on 127E, 45N at 1200 UTC 29, which had extremely cold air below -42°C (Fig. 3a). As time elapsed, the cold vortex moved slowly southward and reached the root of Korean Peninsula at 1200 UTC 30 (Figs. 3b and 3c). A short wave trough having a horizontal scale of 1000 km propagated around the cold vortex from 121E at 1200 UTC 29 to 133E at 1200 UTC 30. As sociated with this short wave trough, a meso-α-scale low at surface existed over the Yellow Sea, and another weak depression over the Japan Sea (not analyzed in the weather map with pressu re contour lines for each 4 hPa) at 1200 UTC 29 (Fig. 4a). The meso-α-scale low decayed before 0000 UTC 30, while the weak depression started to appear on the weather map at the surface at 0000 UTC 30 (Fig. 4b) and developed rapidly over the Japan Sea: Its central surface pressure decreased from 1004 hPa at 0000 UT C 30 to 990 hPa at 0000 UTC 31 (Figs. 4c and 4d).

More detailed surface pressure maps prepared from MANAL (Fig. 5) demonstrate that the meso-α-scale low was accompanied by a surface trough, which extended westward from the center of the low and gradually rotated anticlockwise. The trough was collocated with the cloud band, described in section 2b, on which the MBVD was formed. Another surface trough corresponding to the JPCZ extended from the root of the Korean Peninsula to San-in district (Fig. 5f). These February 1997 studied by Fu et al. (2005)

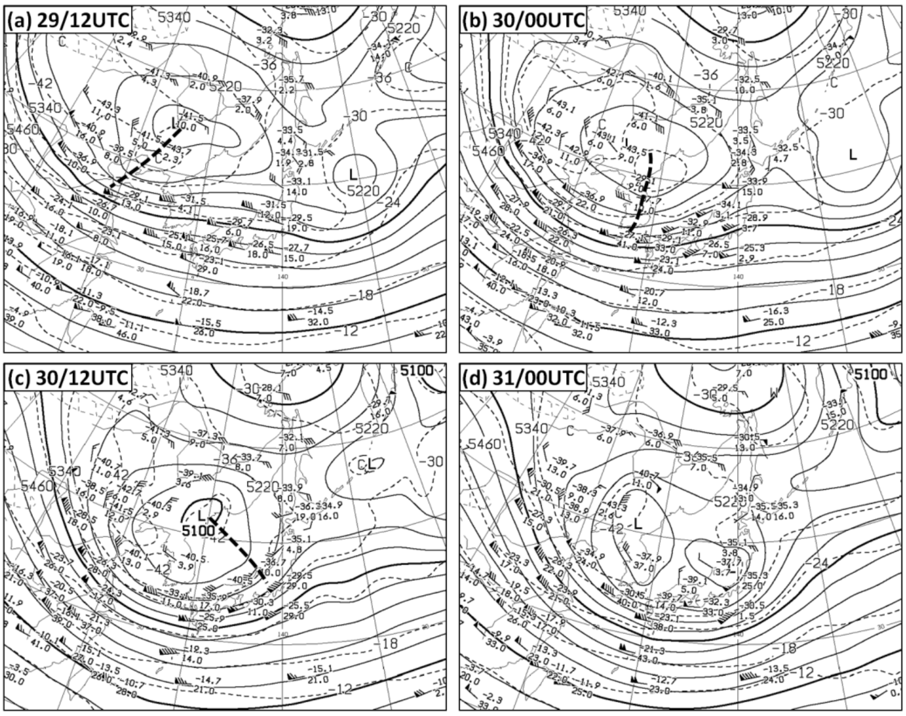

Figure 3. Weather maps at 500 hPa. (a): 1200 UTC 29 Dec 2010, (b): 0000 UTC 30, (c): 1200 UTC 30, and (d): 0000 UTC 31. The thick broken lines in (a), (b) and (c) indicate the short wave trough.

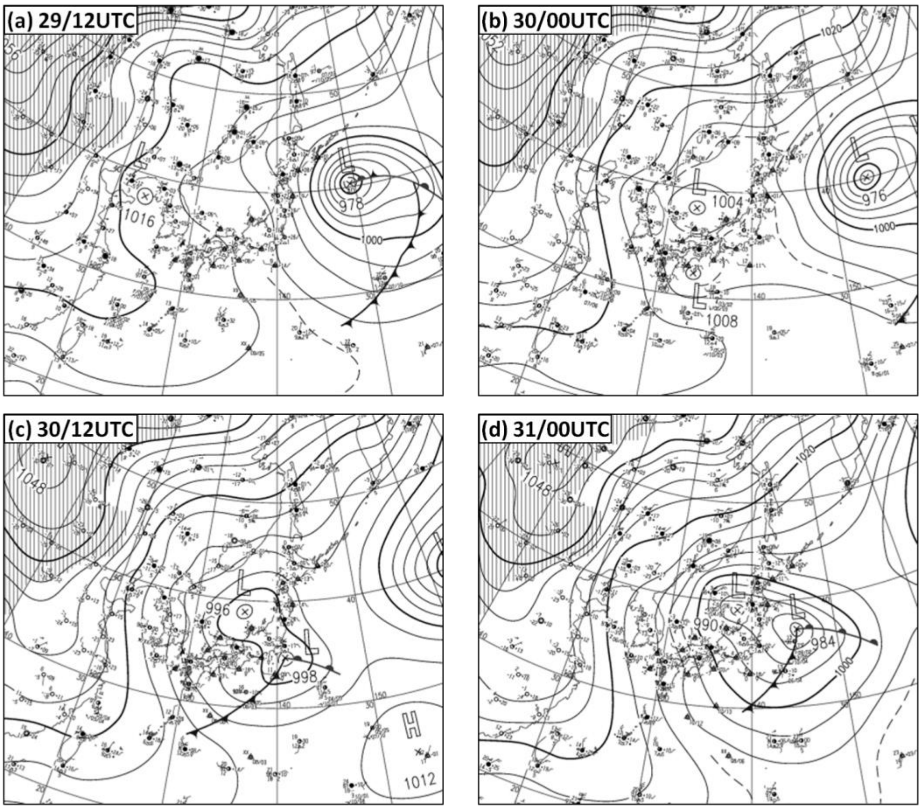

Figure 4. Weather maps at surface. (a): 1200 UTC 29 Dec 2010, (b): 0000 UTC 30, (c): 1200 UTC 30, and (d): 0000 UTC 31.

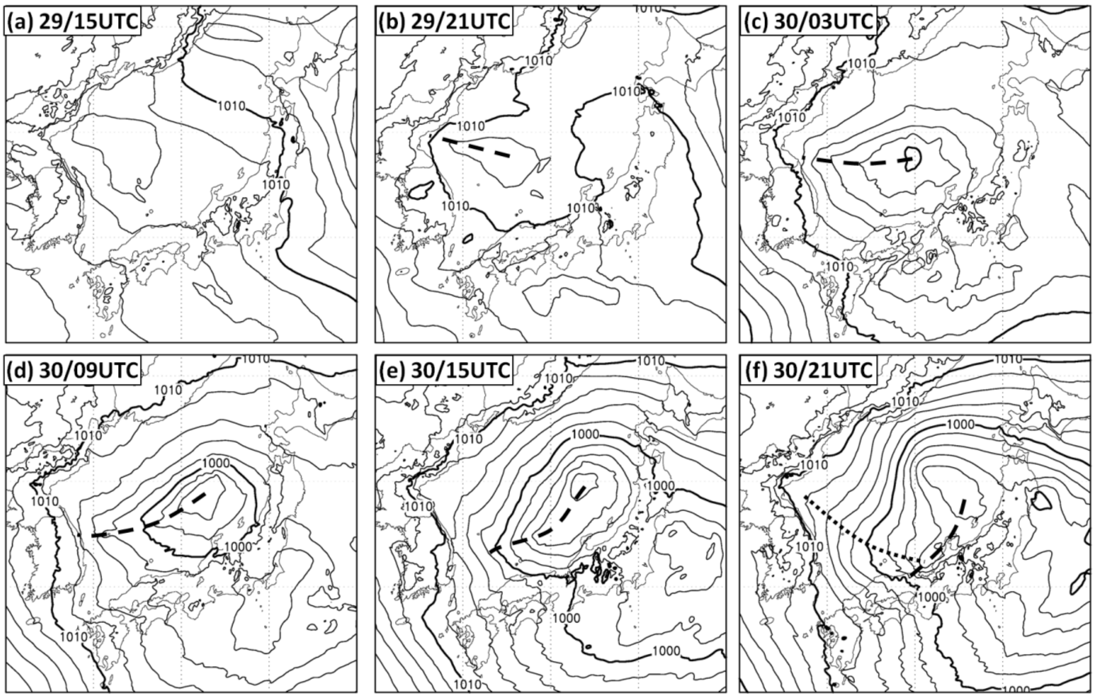

Figure 5. Sea surface pressure. (a): 1500 UTC 29 Dec 2010, (b): 2100 UTC 29, (c): 0300 UTC 30, (d): 0900 UTC 30, (e): 1500 UTC 30, and (f): 2100 UTC 30. The thick broken lines in (b)-(f) indicate the surface trough and dotted line in (f) the JPCZ.

features are similar to the case on 11 except that the JPCZ formed behind the MBVD in the present case.

3. Model description

In order to understand detailed mechanisms of the genesis and development of the MBVD, we have performed a numerical simulation by Japan Meteorological Agency Non-Hydrostatic Model (JMA-NHM). The model domain is 1500 km in the horizontal directions and 15.64 km in the vertical (Fig. 1). The horizontal resolution is 2 km, and the vertical grid interval increases from 40 m near the surface to 823 m near the model top, where 40 grid points are distributed in the vertical direction.

The specification of JMA-NHM used in this study is summarized in Table 1. Cumulus parameterization is not used. A 3-ice single moment bulk scheme (Lin et al. 1983) is used for microphysics and the MYNN level-3 scheme (Nakanishi and Niino 2006) for boundary-layer parameterization. JMA meso-scale model initial time data for each 3 hours are used for initial and boundary conditions. The numerical simulation is started at 0900 UTC 29 December 2010 when the cloud band was not formed and is continued for 48 hours.

4. Results

4.1. Evolution of simulated MBVD and JPCZ

Figure 6 shows simulated wind vectors and relative vorticity fields at 20 m above ground level (AGL) from 1800 UTC 29 to 1700 UTC 30 December 2010, and Figure 7 shows vertically integrated condensed water content and sea level pressure (SLP) fields. At 1800 UTC 29, an ESE-WNW oriented high-vorticity shear zone (SZ-A) which has maximum relative vorticity of 1×10^{-3} s^{-1} is seen around 38.8N (Fig. 6a). It bends southeastward at 131.8E, 39.7N. Cloud region which seems to consist of roll convection spreads in the northeastern side of SZ-A, while no cloud is seen in its southern side (Fig. 7a). SZ-A corresponds to the cloud band found in satellite image (Fig. 2a) and the trough in surface pressure maps (Fig. 5).

Table 1. Specification of the JMA-NHM.

Vertical coordinate	Terrain-following; 40 levels (finer resolution near the surface).
Model top	15,640 m.
Horizontal domain	750 × 750 grid points with 2 km horizontal resolution.
Moist physics	3-ice single-moment bulk scheme (predicting mixing ratio of cloud water, cloud ice, rain, snow, and graupel) (Lin et al. 1983).
Time integration	Horizontally explicit and vertically implicit for sound waves (Δt = 10s).
Turbulent closure	MYNN level 3 scheme (Nakanishi and Niino, 2006).
Cumulus parameterization	*Not* used.
Surface	Bulk method based on Beljaars and Holtslag (1991).
Initial condition	Prepared from MSM initial time data at 0900 UTC 29 December 2010.
Boundary condition	Radiative boundary condition nested within MSM.
Integration period	48 hours (from 0900 UTC 29 December 2010 to 0900 UTC 31 December 2010).

SZ-A is formed between northeasterly and westerly winds which, respectively, go round the northern and southern sides of the mountains on the north of Korea Peninsula (Mt-A, see Fig. 1 for geographical locations). Another shear zone (SZ-B), which extends northeastward from a vortex around 128.5E 39.4N (Vortex-A), is seen between a region of northwesterly wind, which flows out of a valley of Mt-A, and that of weak wind.

As the cold air outbreak from Siberia intensifies, SZ-A marches southward, while rotating anticlockwise. At 0100 UTC 30, SZ-A is oriented in the E-W direction along the latitude line of 39.4N (Fig. 6b). A number of small vortices, each of which has a horizontal scale of about 10 km and is 30 km apart, are found on SZ-A. The maximum vorticity of the vortices is 2×10^{-3} s^{-1}, which is about two times as large as that of SZ-A. These vortices coincide with the region of the large amount of condensed water, where cumulus convection is active (Fig. 7b). SZ-B has become unclear and vortex-A has decayed. A high-vorticity band extends north-northeastward from the western edge of SZ-A. This high-vorticity band corresponds to the earliest formation stage of the JPCZ.

Vortices on SZ-A repeat mergers and end up with two vortices (Vortex-B and Vortex-C). They have horizontal scales of 50 km and interval of 100 km at 0900 UTC 30 (Fig. 6c). Vortex-C has 3 or 4 vorticity peaks, since it has not completed merging processes yet. Condensed water exists in the arc-shaped region surrounding Vortex-B and Vortex-C (Fig.7c) and is scarce near the centers of the vortices. Note that the long axes of these vortices have an up-shear tilt, which indicates that Vortices-B and C are likely to develop through barotropic instability of the horizontal shear flow associated with SZ-A.

Finally, Vortex-C merges with Vortex-B to form a single MBVD, which is located at 132.6E, 36.4N at 1700 UTC 30 (Fig. 6d). The horizontal scale of MBVD is estimated to be 100 km in the vorticity field and 200 km in the cloud field (Fig.7d). Such a difference of horizontal scale when viewed in different physical quantities is also noted by Nagata (1993). The MBVD has a pressure drop of 5 hPa at its center, a cloud-free eye and spiral-shaped clouds. Although the position of the simulated MBVD is about 200 km west of the observed one, its horizontal scale and cloud features are in good agreement with those of the observed one. Note that a shear zone that later develop into a JPCZ is formed behind the MBVD and extends northwestward, which also agrees with the observation.

We may divide the development phase of the life cycle of the MBVD into 3 stages: the

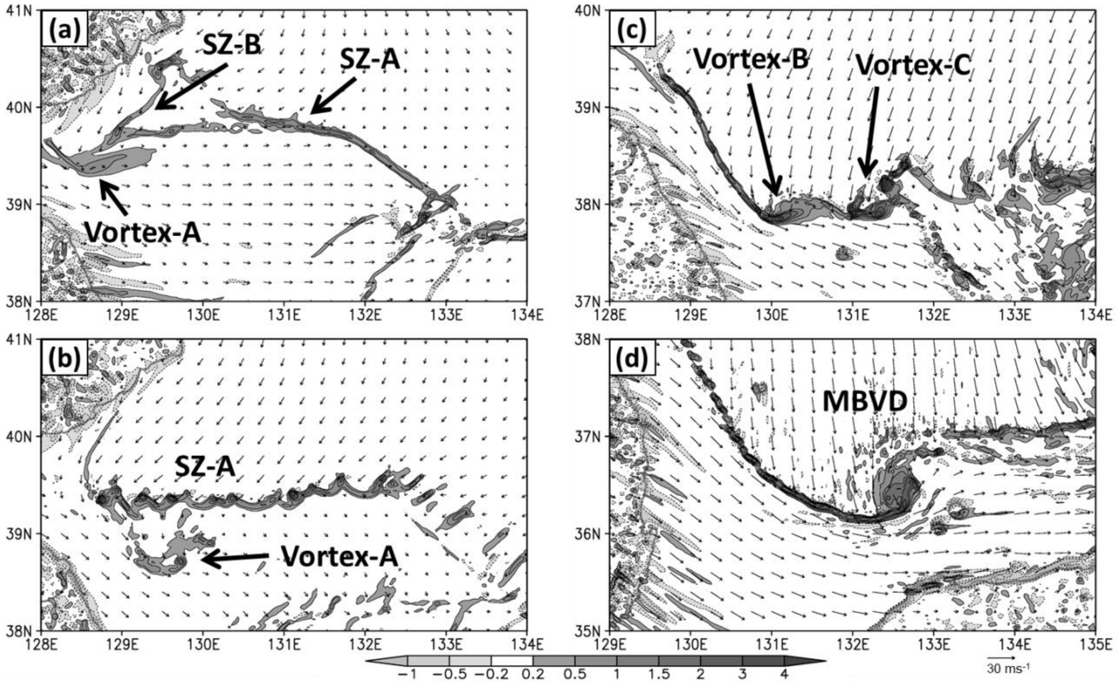

Figure 6. Simulated wind vector and relative vorticity field (1×10^{-3} s^{-1}) at 20 m AGL. (a): 1800 UTC 29 Dec 2010, (b): 0100 UTC 30, (c): 0900 UTC 30, and (d): 1700 UTC 30. Note that the regions shown in each panel are different.

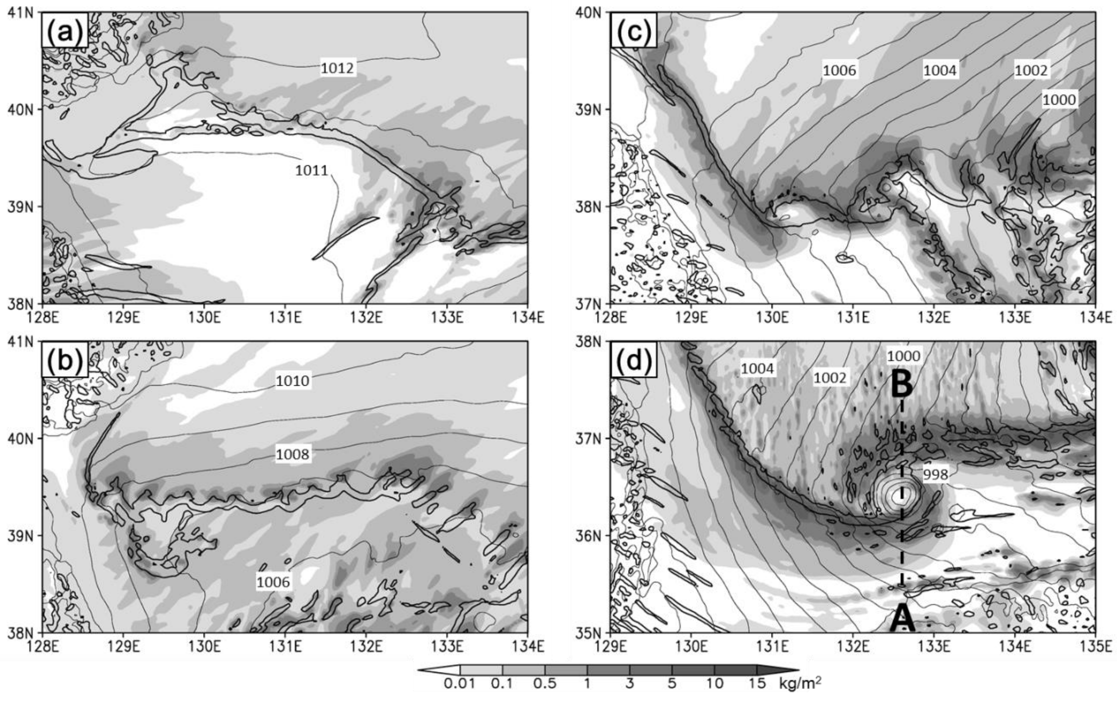

Figure 7. Vertically integrated condensed water content (shaded) and SLP (thin contour). The contour interval is 1 hPa. The thick lines indicate the contour of relative vorticity of 2×10^{-4} s^{-1} at 20m AGL. (a): 1800 UTC 29 Dec 2010, (b): 0100 UTC 30, (c): 0900 UTC 30, and (d): 1700 UTC 30. Note that the regions shown in each panel are different.

early development stage (2000 UTC 29 ~ 0200 UTC 30) in which a number of small vortices appear on SZ-A (Fig. 6b), the late development stage (0200 UTC 30 ~ 1000 UTC 30) in which the merger of the vortices proceeds (Fig. 6c), and the mature stage (1000 UTC 30 ~ 2100 UTC 30) in which only a single MBVD is present (Fig. 6d). We will examine the more detailed structure and development mechanisms of the MBVD at the three stages in the following sections.

4.2. The early development stage

Figure 8 shows close-up views of horizontal wind vector and relative vorticity fields at 20 m, 1122 m, 2147 m and 3133 m AGL at 0100 UTC 30. At 20 m AGL the SZ-A has the width of 10 km and indentations each of which has a bow-shape (Fig. 8a). On the northern edges of SZ-A a number of small vortices which have horizontal scales of about 10 km and intervals of about 30 km exist. At 1122 m AGL SZ-A consists of discrete vortices (Fig. 8b), which are collocated with strong updrafts, while pairs of positive and negative vorticity strips are found by the sides of updrafts at 3133 m AGL (Fig. 8d). The relative vorticity pattern at 2147 m AGL is intermediate between 1122 m and 3133 m AGL (Fig. 8c). Note that wind direction of northern side of SZ-A is northeasterly at 20 m AGL, but changes to southeasterly at 3133 m AGL.

Although barotropic instability is a possible development mechanism of the vortices, the wavelength (i.e. intervals of vortices) is shorter than expected from linear barotropic instability theory: The wavelength of the fastest growing mode is 8 times as long as the width of shear zone (e.g., Gill 1982), which is about 80 km. Furthermore, the vortices have little phase tilt across the shear zone except near the surface. For these reasons, barotropic instability is not likely to account for the development of the vortices.

To examine the development mechanisms of these vortices more in detail, the budget of the eddy kinetic energy is analyzed in the rectangular region as indicated in Figure 8a. We define the x and y coordinates as the directions parallel and perpendicular to SZ-A, and u and v as the wind components in x and y directions, respectively. Now, we consider that any variable η is given by $\eta = \overline{\eta} + \eta'$, where $\overline{\eta}$ is an average along the x-axis and η' is a deviation from the average. A linear trend of potential temperature along the x-axis is removed from θ' to exclude low-wavenumber variation. By ignoring frictional terms, a tendency of the averaged eddy kinetic energy ($\overline{K_E} = \rho_0(\overline{u'^2 + v'^2 + w'^2})/2$) is written as

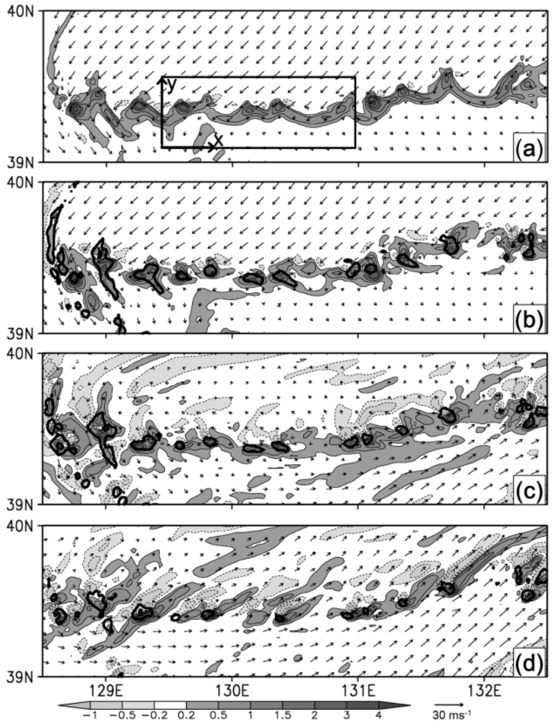

Figure 8. Wind vector and relative vorticity field (1×10^{-3} s^{-1}) at (a): 20 m, (b): 1122 m, (c): 2147 m, and (d): 3133 m AGL at 0100 UTC 30. The thick line indicates the contour of vertical velocity of 0.5 m s^{-1}. The calculation domain used in the energy budget analysis is enclosed by thick black lines in (a).

$$\frac{\partial \overline{K_E}}{\partial t} = \underbrace{-\rho_0\left(\overline{u'v'}\frac{\partial \overline{u}}{\partial y} + \overline{v'v'}\frac{\partial \overline{v}}{\partial y} + \overline{w'v'}\frac{\partial \overline{w}}{\partial y}\right)}_{\mathrm{HSP}} \underbrace{-\rho_0\left(\overline{u'w'}\frac{\partial \overline{u}}{\partial z} + \overline{v'w'}\frac{\partial \overline{v}}{\partial z} + \overline{w'w'}\frac{\partial \overline{w}}{\partial z}\right)}_{\mathrm{VSP}}$$

$$\underbrace{-\left(\overline{v}\frac{\partial\overline{K_E}}{\partial y}+\overline{w}\frac{\partial\overline{K_E}}{\partial z}\right)}_{\text{ADV}}$$

$$\underbrace{-\left(\frac{\partial\overline{u'K_E}}{\partial x}+\frac{\partial\overline{v'K_E}}{\partial y}+\frac{\partial\overline{w'K_E}}{\partial z}\right)}_{\text{ET}}$$

$$\underbrace{-C_p\Theta\left(\frac{\partial\rho_0\overline{u'\pi'}}{\partial x}+\frac{\partial\rho_0\overline{v'\pi'}}{\partial y}+\frac{\partial\rho_0\overline{v'\pi'}}{\partial z}\right)}_{\text{PT}}$$

$$\underbrace{+\frac{\rho_0 g}{\Theta}\overline{\theta' w'}}_{\text{BP}} \qquad (1)$$

where ρ_0 is the horizontal mean density over the rectangular region, g the gravity acceleration, Θ the mean potential temperature, C_P specific heat at constant pressure, and π Exner function. Terms in the right-hand side of eq. (1) may be classified into horizontal shear production terms (HSP), vertical shear production terms (VSP), advection terms (ADV), eddy transport terms (ET), pressure transport terms (PT), and buoyancy production term (BP). Among these terms, HSP, VSP, and BP represent the production of $\overline{K_{\mathrm{E}}}$ and others the transport of $\overline{K_{\mathrm{E}}}$.

Figure 9 shows the vertical cross sections of $\overline{u}$, $\overline{v}$, $\overline{w}$, and $\overline{\theta}$. A strong horizontal shear zone which is tilted northward below 1500 m exists in the $\overline{u}$ field (Fig. 9a). The lower part of this strong shear (below 700 m) corresponds to southward protruded part of SZ-A, while the upper part consists of discrete vortices (Fig. 8). There is also strong vertical shear of $\overline{u}$ around 2500 m. In the $\overline{v}$ field (Fig. 9b), a peak of convergence exists at y = 20 km near the surface. It shifts northward with increasing height and reaches z = 800 m at y = 30 km. On the other hand, a peak of divergence exists at z = 2500 m at y = 30 km. Associated with these peaks of convergence and divergence, two peaks of $\overline{w}$ are found (Fig 9c), although they are located somewhat south of the peaks of convergence and divergence. The peak of $\overline{w}$ at y = 17 km is formed dynamically due to convergence of SZ-A, while that at y = 26 km is caused by buoyancy of cumulus convection. The potential temperature difference across SZ-A

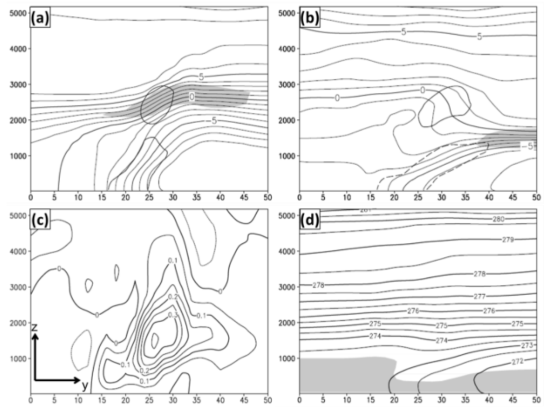

Fig. 9. The vertical cross section of *x*-averaged variables. (a): $\overline{u}$ (contoured at intervals of 1m s^{-1}). The shaded area represents $\partial\overline{u}/\partial z > 8\times10^{-3}\mathrm{s}^{-1}$ and the area surrounded by thick solid contours $\partial\overline{u}/\partial y > 0.5\times10^{-3}\mathrm{s}^{-1}$. (b): $\overline{v}$ (contoured at intervals of 1m s^{-1}). The shaded area represents $\partial\overline{v}/\partial z > 8\times10^{-3}\mathrm{s}^{-1}$ and the area surrounded by thick solid and dashed contours $\partial\overline{v}/\partial y > 0.2\times10^{-3}\mathrm{s}^{-1}$ and $\partial\overline{v}/\partial y < -0.2\times10^{-3}\mathrm{s}^{-1}$, respectively. (c): $\overline{w}$ (contoured at intervals of 0.05m s^{-1}). (d): $\overline{\theta}$ (contoured at intervals of 0.5K). The shaded area represents $\partial\overline{\theta}/\partial z < 0.5K\ \mathrm{km}^{-1}$.

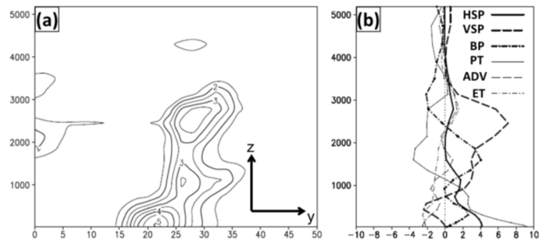

Fig. 10. (a): Vertical cross section of $\overline{K_{\mathrm{E}}}$. (in unit of J m^{-3}). Contour intervals are 0.5 J m^{-3}. (b): The vertical distribution of *y*-averaged HSP, VSP, BP, PT, ADV, and ET in equation (1) (in unit of J m^{-3} s^{-1}).

is about 1 K per 20 km (Fig. 9d). This value is somewhat smaller than that of the real atmosphere because the potential temperature field is smoothed by averaging in the *x*-direction. Because of large sensible heat flux from the sea surface, a nearly neutrally stratified layer is seen below 1000 m in the southern side of SZ-A and below 600 m in the northern side.

Figures 10a and 10b show a vertical cross section of the averaged eddy kinetic energy $\overline{K_{\mathrm{E}}}$ and vertical distributions of each term in the right-hand side of Eq. (1) averaged along y-axis, respectively. A peak of $\overline{K_{\mathrm{E}}}$ is seen below 700 m at y = 21 km (Fig. 10a). This peak seems to be formed through barotropic instability of SZ-A because the HSP term is large below 700 m where large shear of $\bar{u}$ of SZ-A exists (Fig. 9a) and vortices have a slight up-shear tilt (Fig. 8a). The VSP term is negative below 700 m, where the second term of VSP related to vertical shear of $\bar{v}$ is negative and contributes to suppress the growth of $\overline{K_{\mathrm{E}}}$. Such a suppression of the barotropic instability wave by the vertical shear is similar to the results of an idealized experiment on a cold front by Kawashima (2011). The BP term which has a large value around 400 m also contributes to the growth of $\overline{K_{\mathrm{E}}}$

Another peak of $\overline{K_{\mathrm{E}}}$ is found at y = 26 km between 2000 m and 3500 m. This peak is caused mainly by the BP term and the VSP term which have large positive value around 1600 m and 2500 m, respectively. They are closely related to cumulus convection. The BP term is generated by condensational heat in cumulus convection and the VSP term is related to vertical momentum transport by cumulus convection in a strong vertical shear of $\bar{u}$ around 2500 m. The net contribution of the BP term and the VSP term is larger than that of HSP term, indicating that the vortices at the early development stage acquire their energy mainly through cumulus convection. If this process is viewed in the vorticity equation, vorticity increases due to stretching of vertical vorticity associated with horizontal shear and tilting of horizontal vorticity associated with vertical shear by strong updrafts of cumulus convection. This is consistent with the distributions of the vorticity and updrafts.

The depth of cold air which breaks out from Siberia is less than 1000 m and SZ-A has a similar depth. Since the vertical shear is strong above the cold air, a suppression of barotropic instability waves by the vertical shear as suggested by Kawashima (2011) is likely to occur. On the other hand, sensible and latent heat fluxes from the sea surface and the cold vortex aloft bring unstable stratification, which is favorable for cumulus convection. Thus, the cumulus convection contributes more to the development of the vortices than the barotropic instability does, resulting in a smaller horizontal wavelength than expected from the barotropic instability.

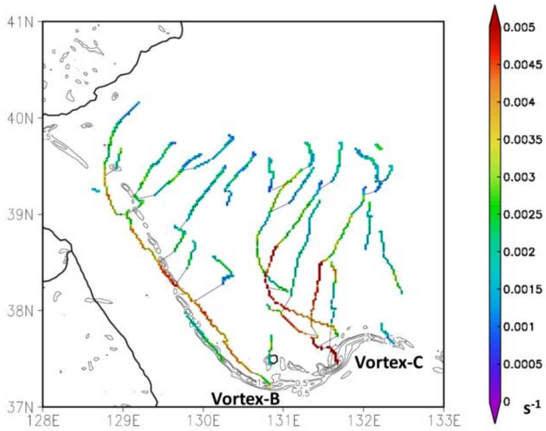

Figure 11. Tracks of vortices from 2000 UTC 29 to 1200 UTC 30. Only the tracks of vortices which can be tracked more than 2 hours are shown. The color indicates the maximum vorticity of each vortex. The vorticity field at 20 m AGL at 1200 UTC 30 is also shown by contours.

4.3. The late development stage

At the late development stage the merger of vortices proceeds. Figure 11 shows tracks of the vortices from 2000 UTC 29 to 1200 UTC 30, where a center of each vortex is determined by a local vorticity maximum. At 2000 UTC 29 the vortex which later develops into Vortex-B is located at 129.2E, 40.2N. It first moves southwestward as its maximum vorticity gradually increases. Then, it changes its direction of movement to southeastward at 0100 UTC 30, while absorbing several vortices which move southwestward to approach it. As the merger proceeds, its maximum vorticity fluctuates and its horizontal scale increases gradually.

On the other hand, it is difficult to identify a vortex which develops into Vortex-C since complicated mergers and generation changes occur repeatedly. Each vortex, which has some connection to Vortex-C, first increases its maximum vorticity, but then starts to decay, and is finally absorbed into another vortex

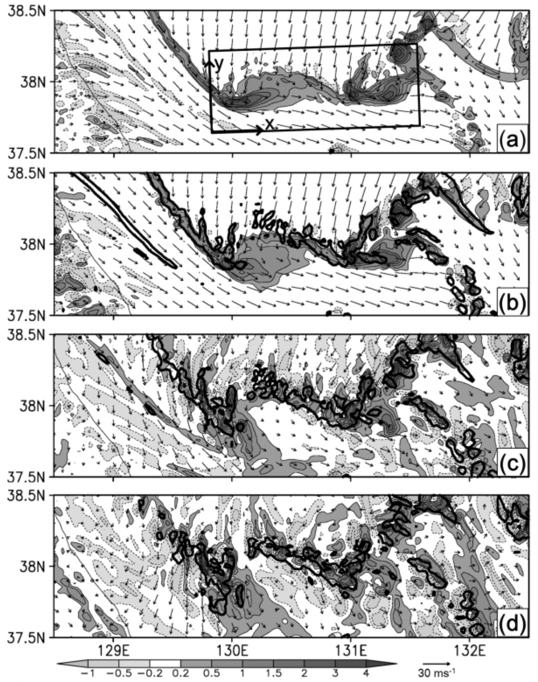

Figure 12. As in Fig. 8 but at 0900 UTC 30.

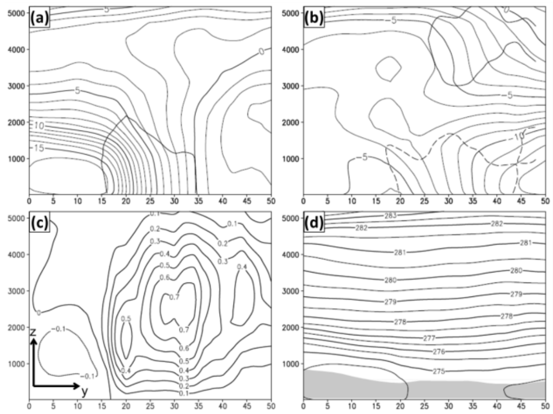

Figure. 13. As in Fig. 9 but at 0900 UTC 30. Contour intervals of $\overline{w}$ are 0.1m s^{-1}rectangular region as indicated in Fig. 12a.

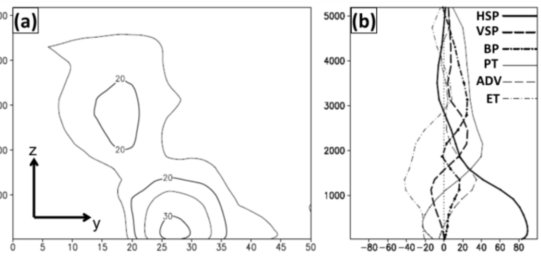

Figure. 14. As in Fig. 10 but at 0900 UTC 30. Contour intervals of $\overline{K_{\mathrm{E}}}$. is 5 J m^{-3}.

which has approached from northeastern direction. The latter vortex then starts to develop next. As the similar processes are repeated, the horizontal scale of Vortex-C increases gradually. Similar mergers and development of vortices are also found in the numerical experiment by Kawashima (2005).

Close-up views of the horizontal wind vector and relative vorticity fields at 20 m, 1122 m, 2147 m, and 3133 m AGL at 0900 UTC 30 are shown in Fig. 12. Vortices-B and C have maximum vorticity exceeding 3×10^{-3} s^{-1} (Fig. 12a). The horizontal scale of Vortices-B and C, and their interval are 50 km and 100 km, respectively. They are connected by a filament of high vorticity exceeding 0.2×10^{-3} s^{-1}. Similar features are also seen at 1122 m (Fig. 12b). Although the interval of the vortices is a little shorter than the wavelength of the fastest growing mode (about 160 km) predicted from linear barotropic instability theory, the long axes of these vortices have an up-shear tilt, suggesting that Vortices-B and C gain their energy from barotropic instability of the horizontal shear flow associated with SZ-A. Above 2000 m AGL Vortices-B and C become obscure, and pairs of positive and negative vorticity, which are likely to be formed by tilting of horizontal vorticity associated with vertical shear, are found (Figs. 12c and 12d).

The budget of eddy kinetic energy at 0900 UTC 30 is also analyzed in the rectangular region as indicated in Fig. 12a. The large horizontal shear of $\bar{u}$ corresponding to SZ-A is seen below about 1500 m (Fig. 13a), which is higher than that at 0100 UTC (Fig. 9a). The increase of the depth of SZ-A is due to the development of the convective mixed layer through airmass transformation. In the $\bar{v}$ field (Fig. 13b), both convergence and divergence are intensified, where the divergence is located about 4000 m. The updraft reaches up to 5000 m (Fig. 13c), which indicates that cumulus convection becomes more active. The potential temperature gradient across SZ-A becomes smaller than that at the early development stage (Fig. 13d).

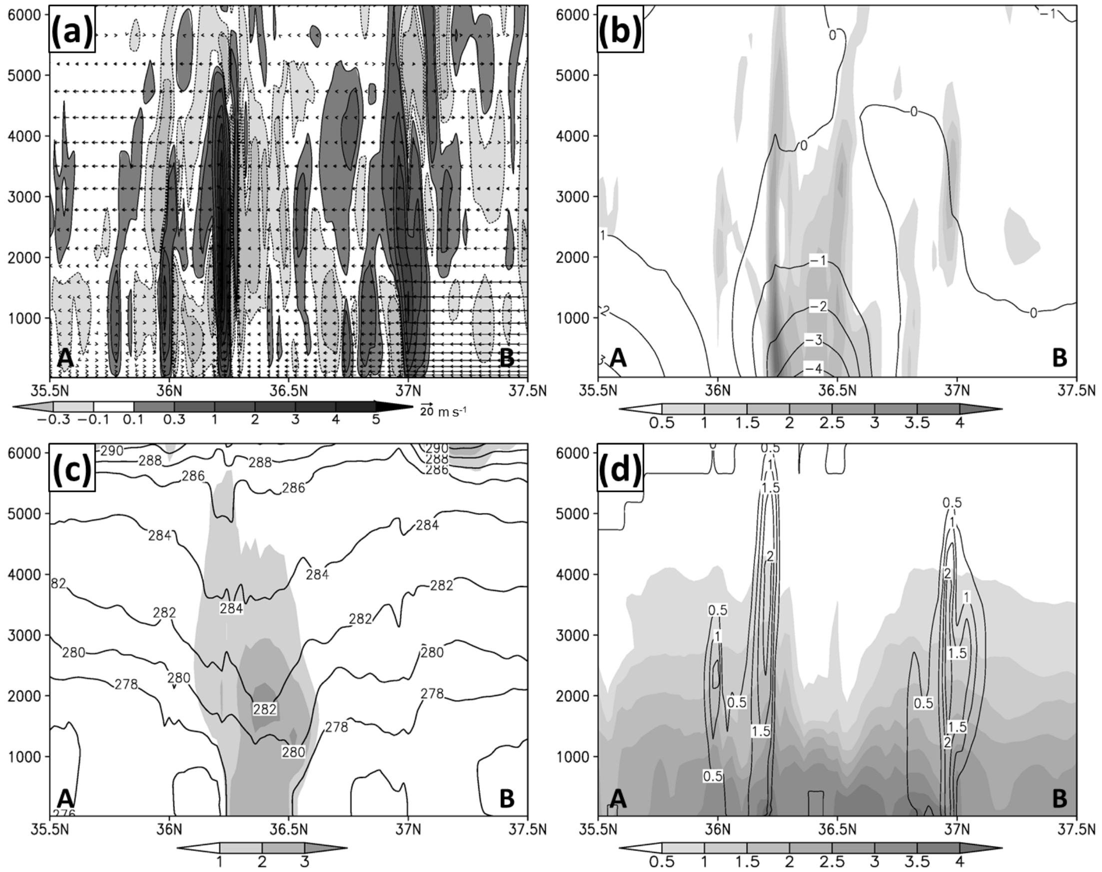

Figure 15. Vertical cross section along the line AB in Fig.7d. (a) vertical velocity (shaded; m s^{-1}) and meridional wind (vector), (b): pressure anomaly from meridional average (contour; hPa) and relative vorticity (shaded; s^{-1}), (c): potential temperature (contour; K) and its deviation from meridional average (shaded; K), and (d): mixing ratio of condensed water i.e. cloud, cloud ice, rain, snow, and graupel q_c+ q_{ci}+ q_r+ q_s+ q_g (contour; g kg^{-1}) and mixing ratio of water vapor q_v (shaded; g kg^{-1})

The distribution of $\overline{K_{\mathrm{E}}}$ has a peak extending from the surface to 1500 m at y = 25 km (Fig. 14a). The amplitude of $\overline{K_{\mathrm{E}}}$ is about 6 times as large as that at 0100 UTC (Fig. 10a). The horizontal shear production (HSP) term is dominant below 1500 m (Fig. 14b), corresponding to the large horizontal shear (Fig. 13a) and the horizontal convergence (Fig. 13b). Although vertical shear production (VSP) and buoyancy production (BP) terms have also increased from 0100 UTC, their increases are smaller than that of HSP term (cf. Fig. 10b). These results indicate that the vortices acquire their energy mainly through the barotropic instability process at the late development stage. The increase of the depth of SZ-A makes the relative contribution of horizontal shear dominant over that of cumulus convection. Note that the peak of $\overline{K_{\mathrm{E}}}$ at 3000 m is not physically meaningful since the flows above 1500 m AGL are far from two-dimensional (Figs. 12c and 12d).

4.4. The mature stage

Vortex-C absorbs Vortex-B to form a single MBVD having a cloud-free eye at the mature stage (Figs. 6d and 7d). The SLP field and cloud pattern demonstrate that the MBVD has a nearly axisymmetric shape. Figure 15 shows vertical cross sections along the line AB in Fig. 7d. There are strong updrafts extending up to 5000 m with a maximum value of 5 m s^{-1} in both south and north sides of the center of the MBVD (around 36.4N)

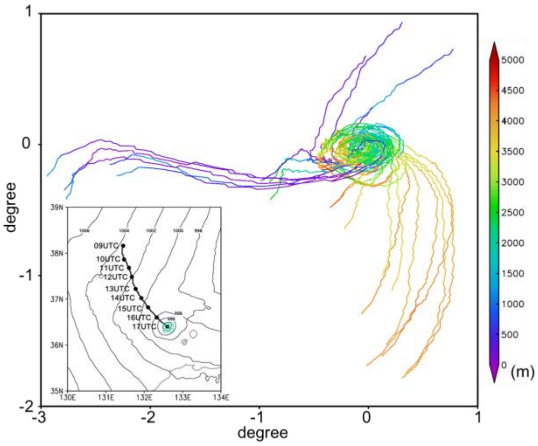

Figure 16. Trajectories of parcels relative to the MBVD. The plot is made in order to keep the center of the MBVD at (0, 0). Colors on each trajectory indicate parcel height. The track of the MBVD is shown in the left bottom panel together with the contour of SLP at 1700 UTC 30. The dots in this panel indicate the position of parcels at 1700 UTC 30.

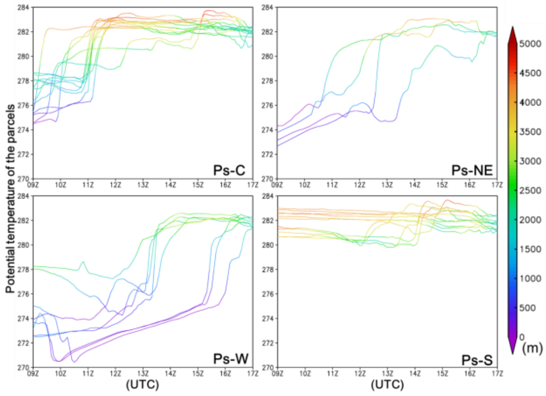

Figure 17. Time series of potential temperatures of parcels. The line color indicates parcel height. (Fig. 16).

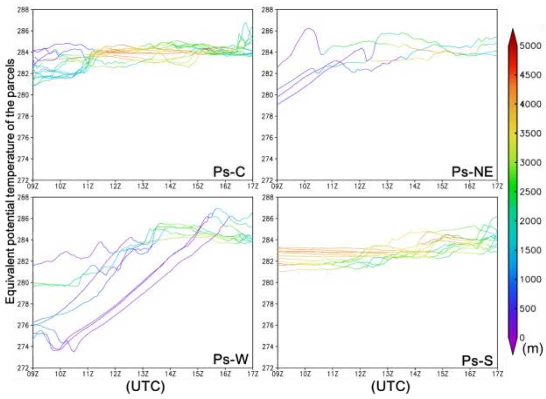

Figure 18. As in Fig. 17 but for equivalent potential temperature.

(Fig. 15a). They correspond to cumulus clouds in the spiral-cloud bands surrounding the eye. There is also meridional circulation in which convergence and divergence are seen at lower- and upper- levels, respectively. The thickness of an inflow layer near the surface is about 2000m which almost matches the depth of the mixed layer. A weak downdraft with a maximum value of 0.5 m s^{-1} exists at the center of the MBVD. The potential temperature field (Fig. 15c) shows a significant warm core structure, where the core is 3K warmer than the surroundings at around 2000 m AGL. The distribution of water vapor mixing ratio q_v demonstrates that dry air occupies the center of the MBVD (Fig. 15d), where downdraft is dominant. These distributions of vertical velocity, potential temperature and q_v imply that the warm core and cloud-free eye structure are formed by adiabatic heating associated with the downdraft. The pressure anomaly, which is in gradient wind balance with rotational wind, decreases toward lower levels, where the vorticity is larger (Fig. 15b). The resulting downward pressure gradient force causes the downdraft.

In order to examine the formation process of the warm core in more detail, a backward trajectory analysis is conducted. 36 parcels are distributed at 2000 m AGL around the center of the warm core (36.28N-36.48N, 132.5E-132.75E) at 1700 UTC 30, and their backward trajectories are obtained for 8 hours

The model outputs with 5 minute intervals are used for the backward integration, where the forward Euler method with a time step of 10 seconds is adopted. The velocity components at each point on the trajectory are calculated by linearly interpolating the model outputs spatially and temporally. The potential temperatures and equivalent potential temperatures of the parcels are also calculated with the same interpolation method.

The trajectory analysis reveals that the parcels which have reached the warm core are originally located in four regions relative to the vortex center: near the vortex center, and northeastern, western, and southern sides of the vortex (Fig. 16). Hereafter, the parcels in these regions are referred to as Ps-C, Ps-NE, Ps-W, and Ps-S, respectively. Ps-C are advected together with the vortex, while other parcels are gradually taken into the vortex and then move with it. Most of Ps-C, Ps-NE, and Ps-W are located at low levels at 0900 UTC. While they travel at low levels, their potential temperatures and equivalent potential temperature gradually increase due to sensible and latent heat fluxes from the sea surface (Figs. 17 and 18). Then they rapidly ascend as they approach the vortex. During this rapid ascent, the potential temperatures of the parcels also increase quickly (Figs. 17a-c), while nearly conserving equivalent potential temperatures (Figs. 18a-c). This implies that the rapid ascent is caused by updrafts in cumulus convection which is accompanied by diabatic heating. Parcels raised by cumulus convection eventually descend into the warm core and account for about two-thirds of all parcels. On the other hand, Ps-S are originally located at upper levels, and descend into the warm core while conserving their potential temperatures and equivalent potential temperatures (Figs. 17d and 18d). These results confirm that the warm core is formed by adiabatic heating associated with downdrafts.

The structure of the MBVD at the mature stage depicted above resembles a tropical cyclone or a polar low with little baroclinicity (e.g. M0 case in Yanase and Niino 2007), which indicates that the MBVD may develop through CISK/WISHE mechanism. It is known that CISK/WISHE mechanism can operate only when the initial vortex is strong enough (Emanuel and Rotunno 1989; Yanase and Niino 2007). In the present case, the MBVD appears to change its developing mechanism from shear instability to CISK/WISHE after it reaches a threshold strength. Note that Yokota et al. (2012) reported a similar analysis about tropical cyclogenesis associated with an ITCZ breakdown in which the development mechanism of the vortex transitioned from barotropic instability to CISK/WISHE.

5. Sensitivity experiments

As described in the previous section, the MBVD in the present study is generated on a shear zone as an array of small vortices associated with individual cumulus clouds at the early development stage, develops through barotropic instability at the late development stage, and finally develops through CISK or WISHE mechanism at the mature stage. It is inferred that the contributions of the physical processes such as condensational heating and heat fluxes from sea surface to the development of the MBVD can be different at each stage. In order to examine which physical process affects the development of the MBVD at each stage, sensitivity experiments are performed.

In the sensitivity experiments, the model setting is the same as described in section 3 except that sensible and latent heat fluxes from the sea surface and condensational heating are switched on/off. Six experiments (CTL, DRY, NO_SH, NO_LH, NO_SLH, and NO_SLH_DRY) as shown in Table 2 are

Table. 2. Setting and naming of the six sensitivity experiments.

Experiment name	Physical process considered
CTL	Control run with all the physical processes included
DRY	No condensational heating
No_SH	No sensible heat flux from the sea surface
No_LH	No latent heat flux from the sea surface
No_SLH	No heat fluxes from the sea surface
No_SLH_DRY	No condensational heating and no heat flux from the sea surface

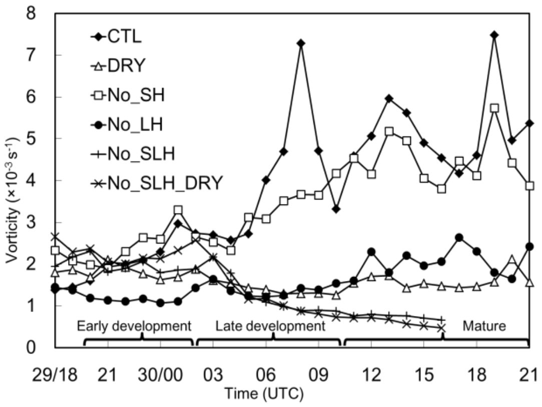

Figure 19. Time evolutions of maximum vorticity at 20 m AGL for the 48h sensitivity experiments.

performed. CTL denotes the experiment described in the previous section. Condensational heating is switched off in DRY. In No_SH, No_LH, and No_SLH, sensible heat flux, latent heat flux and both of them are removed, respectively. In No_SLH_DRY all of these three processes are switched off.

Two types of sensitivity experiments have been performed. One is named "48h experiment" in which the physical processes are switched on/off throughout the whole integration time of 48 hours. The other is "9h experiment" in which the physical processes are switched on/off only for 9 hours after 0900 UTC 30 (24 hours after the start of the integration).

5.1. 48h experiments

Figure 19 shows the time evolutions of the maximum relative vorticity at 20 m AGL in the MBVD between 1800 UTC 29 and 2100 UTC 30 for the 48h experiments. Shear zones corresponding to SZ-A in CTL are formed in all experiments at 1800 UTC 29 (not shown). The maximum relative vorticity in CTL gradually increases at the early development stage, rapidly increases at the late development stage, and fluctuates around the value of 5×10^{-3} s^{-1} at the mature stage. The maximum vorticity in No_SH displays a similar time evolution to that in CTL, although it is a little smaller. In contrast, the maximum vorticities in DRY and No_LH do not increase during the integration. The vortices and shear zones in No_SLH and No_SLH_DRY have disappeared during the integration.

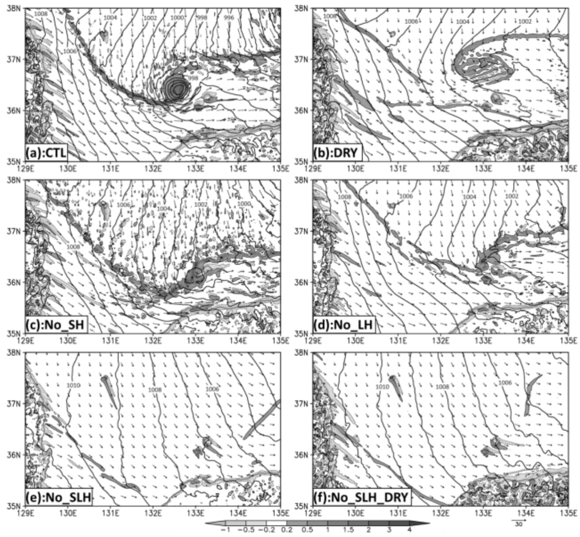

Figure 20. Wind vector and relative vorticity (shaded; 1×10^{-3} s^{-1}) at 20 m AGL and SLP (contour interval is 1 hPa) at 1700 UTC 30 for 48h sensitivity experiments. (a): CTL, (b): DRY, (c): No_SH, (d): No_LH, (e): No_SLH, and (f): No_SLH_DRY.

The other characteristics of the vortices in No_SH are also similar to that of CTL; generation of small vortices on a shear zone at the early development stage (not shown), merger of vortices and larger vortices at the late development stage (not shown), and a MBVD with pressure depression at the mature stage (Fig. 20c) are also simulated in No_SH. This result indicates that condensational heating associated with cumulus convection is crucial to the development of the MBVD. The fact that the difference between CTL and No_SH is small implies that sensible heat flux plays a secondary role in the development of MBVD, although it contributes to make the environment favorable for cumulus convection by destabilizing stratification in the lower layer and also for horizontal shear instability by increasing the depth of the shear zone.

In No_LH vorticity does not increase, although condensational heating is included. Since cold airmass from Siberia contains little

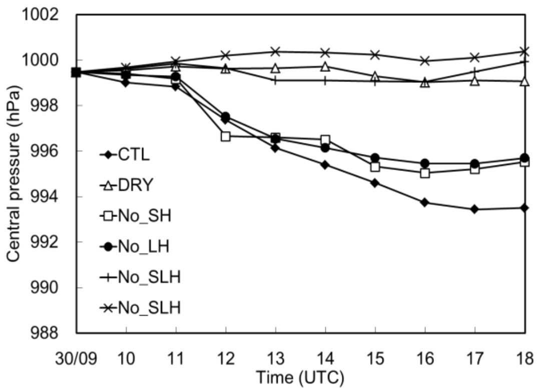

Figure 21. Time evolutions of central pressure of the MBVD for the 9h sensitivity experiments.

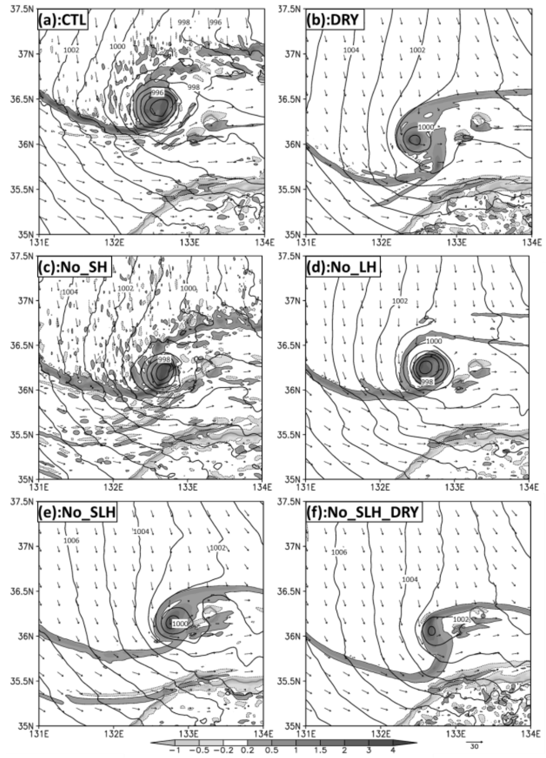

Figure 22. As in Fig. 21 but for 9h sensitivity experiments.

water vapor, condensation hardly occurs without a supply of water vapor from the sea surface, resulting in a similar time evolution to that in DRY. In these two experiments of NO_LH and DRY, wavelike structures with longer wavelengths than the interval of the small vortices in CTL and No_SH are observed at the early and late development stage (not shown). These wavelike structures are likely to be caused by barotropic instability on the shear zone and eventually roll up to form a vortex (Figs.20b and 20d), though its maximum vorticity does not increase. Similar wavelike structures are also seen in No_SLH and No_SLH_DRY, but they as well as the shear zone decay soon (Figs.20e and 20f).

5.2. 9h experiments

As mentioned in Yanase et al. (2004), a removal of a certain physical process for a long time as in the 48h experiments deforms not only the vortex itself but also the environment in which the vortex develops. In fact, the meso-α-scale low which is located to the east of the MBVD is deformed in the 48h experiments, so that the cold air outbreak in which the MBVD develops is changed. In order to examine the effect of physical processes on the MBVD at the mature stage while keeping the deformation of the environment as small as possible, we have performed 9h experiments.

Figure 21 shows the time evolutions of the central pressure of the MBVD from 0900 UTC 30 to 1800 UTC 30 for six sensitivity experiments. The MBVD in CTL have the lowest central pressure among the six experiments. The central pressure of the MBVD in No_SH and that in No_LH also decrease, although they are somewhat higher than that in CTL. The patterns of the SLP and vorticity fields in these two experiments are similar to that in CTL (Figs. 22c and 22d). On the other hand, the central pressures in DRY, No_SLH, and No_SLH_DRY do not decrease at all (Figs. 22b, 22e and 22f). These results indicate that condensational heating is also crucial to the development of the MBVD at the mature stage.

In contrast to the 48h experiment, the MBVD in No_LH develops in the 9h experiment. Since there is abundant water vapor around the MBVD at the beginning of the 9h experiment, cumulus convection can be maintained by collecting this ambient water vapor during the relatively short period of 9 hours, suggesting that the development mechanism of the MBVD at the mature stage is likely to CISK rather than WISHE. On the other hand, the MBVD in No_SLH does not develop. Removing sensible heat flux in addition to latent heat flux brings very stable stratification in the lower layer, resulting in a suppression of cumulus convection.

6. Summary

An MBVD observed on 30 December 2010 is studied by means of an observational analysis and numerical simulations. Although MBVDs are often formed on a pre-existing JPCZ, the present MBVD formed without a presence of a JPCZ, which was rather generated behind the MBVD.

First we analyzed observational data. Satellite images show that, prior to the development of the MBVD, a chain of vortices appeared on an east-west oriented cloud band. This cloud band corresponded to a trough extended westward from a meso-α-scale low which moved eastward over the Japan Sea. The vortices eventually merged into a MBVD which had a horizontal scale of about 150 km and had a cloud-free eye and spiral-cloud bands. A JPCZ was formed behind the MBVD.

A numerical simulation using JMA-NHM of 2 km horizontal mesh, which was started before the east-west oriented cloud band was formed, successfully reproduced the observed MBVD. The results of the numerical simulation suggest that the development phase of the MBVD may be divided into 3 stages: the early development stage in which a number of small vortices appear on a shear zone, the late development stage in which the merger of vortices proceeds and a few larger vortices are formed, and the mature stage in which only a single MBVD is present.

We performed an eddy kinetic energy budget analysis to examine the development mechanisms of vortices at the early and late development stages. It reveals that, at the early development stage, horizontal shear production (HSP) is confined to low-levels and is smaller than buoyancy production (BP) and vertical shear production (VSP) in upper-levels, where both of BP and VSP are related to cumulus convection. This result indicates that vortices at the early development stage acquire their energy from discrete cumulus convection. At the late development stage, on the other hand, HSP becomes relatively dominant since the depth of the shear zone increases as the mixed layer develops, and the vortices develop through barotropic instability.

The structure of the MBVD at the mature stage is also examined in detail. The simulated MBVD is accompanied by a cloud-free eye and spiral-cloud bands. A warm core structure is seen at the center of the MBVD, where a dry downdraft occupies. A backward trajectory analysis confirms that the warm core is formed due to adiabatic heating by the downdraft. Such a structure of the MBVD resembles to a tropical cyclone, which develops through a thermal instability such as CISK.

In order to examine the effects of physical processes on the development of the MBVD, we performed sensitivity experiments in which sensible and latent heat fluxes from the sea surface and condensational heating are switched on/off. Two types of sensitivity experiments have been performed. One is named “48h experiment” in which the physical processes are switched on/off throughout the whole integration time of 48 hours. The other is “9h experiment” in which the physical processes are switched on/off only for 9 hours after 0900 UTC 30. 48h experiments demonstrate that the condensational heating is essential to the development of the MBVD. The sensible heat flux plays a secondary role, although it contributes to make the environment favorable for cumulus convection by destabilizing stratification in the lower layer and also for horizontal shear instability by increasing the depth of the shear zone. The latent heat flux moistens the environment and makes it favorable for cumulus convection. 9h experiments indicate that condensational heating is also essential for the development at the mature stage. The effect of horizontal convergence of pre-existing water vapor also plays some important role in the development.

The present study examined only a single MBVD in detail. However, the genesis and development processes of meso-scale vortical disturbances over the Japan Sea differ significantly from case to case. Therefore further case studies are needed in order to acquire a complete understanding on the vortical disturbances.

References

Asai, T., 1988: Meso-scale features of heavy snowfalls in Japan Sea coastal regions of Japan (in Japanese). *Tenki*, **35,** 156-161.

Asai, T., and Y. Miura, 1981: An analytical study of meso-scale vortex-like disturbances observed around Wakasa Bay area. *J. Meteor. Soc. Japan*, **59,** 832-843.

Beljaars, A. C. M., and A. A. M. Holtslag, 1991: Flux parameterization over land surfaces for atmospheric models. *J. Appl. Meteor.*, **30,** 327-341.

Emanuel, K. A., and R. Rotunno, 1989: Polar lows as arctic hurricanes. *Tellus*, **41A,** 1-17.

Fu, G., H. Niino, R. Kimura, and T. Kato, 2004: Multiple polar mesocyclones over the Japan Sea on 11 February 1997. *Mon. Wea. Rev.*, **132,** 793-814.

Gill, A. E., 1982: *Atmosphere-Ocean Dynamics.* Academic Press, 662 pp.

Hjelmfelt, M. R., 1990: Numerical study of the influence of environmental conditions on lake-effect snowstorms over Lake Michigan. *Mon. Wea. Rev.*, **118,** 138-150.

Kato, T., 2005: Momentum energy budget analysis on a vortex disturbance developing along the Japan-Sea Polar-Airmass Convergence Zone (in Japanese). *Meteor. Res. Note*, **208,** 277-284.

Kawashima, M., 2005: The basic numerical experiment of vortex snowfall cloud generated on the horizontal wind shear line (in Japanese). *Meteor. Res. Note*, **208,** 285-292.

Kawashima, M., 2011: Numerical study of horizontal shear instability waves along narrow cold frontal rainbands. *J. Atmos. Sci.*, **68,** 878-903.

Kawashima, M., and Y. Fujiyoshi, 2005: Shear instability wave along a snowband: Instability structure, evolution, and energetics derived from dual-Doppler radar data. *J. Atmos. Sci.*, **62,** 351-370.

Kuroda, Y., 1992: The convergent cloud band and shipwreck in the Japan Sea (in Japanese). *Sea Sky*, **67,** 261-279.

Laird, N. F., L. J. Miller, and D. A. R. Kristovich, 2001: Synthetic dual-Doppler analysis of a winter mesoscale vortex. *Mon. Wea. Rev.*, **129,** 312-331.

Lee, T. Y., Y. Y. Park, and Y. L. Lin, 1998: A numerical modeling study of mesoscale cyclogenesis to the east of the Korean Peninsula. *Mon. Wea. Rev.*, **126,** 2305-2329.

Lin, Y. L., R. D. Farley, and H. D. Orville, 1983: Bulk parameterization of the snow field in a cloud model. *J. Climate Appl. Meteor.* , **22,** 1065-1092.

Maejima, Y., and K. Iga, 2011: The time evolution of meso-scale disturbances in the atmosphere caused by frontal instability. *Theoretical and Applied Mechanics Japan*, **60,** 183-191.

Miyazawa, S., 1967: On vortical mesoscale disturbances observed during the period of heavy snow or rain in the Hokuriku district. *J. Meteor. Soc. Japan*, **45,** 166-176.

Nagata, M., 1993: Meso-β-scale vortices developing along the Japan-Sea Polar-Airmass Convergence Zone (JPCZ) cloud band: Numerical-simulation. *J. Meteor. Soc. Japan*, **71,** 43-57.

Nakai, S., and S. Yamaguchi, 2012: Snowfall characteristics and the occurrence of related disasters during the heavy snowfall in 2010/2011 winter -Overview in whole Japan and the concentrated heavy snowfall in Tottori-. *Natural Disaster Research Report*, **47,** 1-16.

Nakanishi, M., and H. Niino, 2006: An improved Mellor-Yamada level-3 model:

Its numerical stability and application to a regional prediction of advection fog. *Bound-Layer Meteor.*, **119,** 397-407.
Ninomiya, K., 1989: Polar/comma-cloud lows over the Japan Sea and the northwestern Pacific in winter. *J. Meteor. Soc. Japan*, **67,** 83-97.
Ninomiya, K., and K. Hoshino, 1990: Evolution process and multi-scale structure of a polar low developed over the Japan Sea on 11-12 December 1985. Part II: Meso-β-scale low in meso-α-scale polar low. *J. Meteor. Soc. Japan*, **68,** 307-318.
Ninomiya, K., K. Hoshino, and K. Kurihara, 1990: Evolution process and multi-scale structure of a polar low developed over the Japan Sea on 11-12 December 1985. Part I: Evolution process and meso-α-scale structure. *J. Meteor. Soc. Japan*, **68,** 293-306.
Ookubo, A., 1997: Structure of a mesoscale vortex formed off the Hokuriku district in the winter cold-air outbreak: A case study of the Keifu-maru intensive observation on 5 February 1995 (in Japanese). *Tenki*, **44,** 241-250.
Rasmussen, E., 1979: The polar low as an extratropical CISK Disturbance. *Quart. J. Roy. Meteor. Soc.*, **105,** 531-549.
Rasmussen, E., and J. Turner, 2003: *Polar Lows.* Cambridge University Press, 612pp.
Reed, R. J., and C. N. Duncan, 1987: Baroclinic instability as a mechanism for the serial development of polar lows. *Tellus*, **39A,** 376-384.
Tsuboki, K., and G. Wakahama, 1992: Mesoscale cyclogenesis in winter monsoon air streams: Quasi-geostrophic baroclinic instability as a mechanism of the cyclogenesis off the west-coast of Hokkaido Island, JAPAN. *J. Meteor. Soc. Japan*, **70,** 77-93.
Tsuboki, K., and T. Asai, 2004: The multi-scale structure and development mechanism of mesoscale cyclones over the Sea of Japan in winter. *J. Meteor. Soc. Japan*, **82,** 597-621.
Yamagishi, Y., M. Doi, N. Kitabatake, and H. Kamiguchi, 1992: A polar low which accompanied strong gust (in Japanese). *Tenki*, **39,** 27-36.
Yanase, W., and H. Niino, 2007: Dependence of polar low development on baroclinicity and physical processes: An idealized high-resolution numerical experiment. *J. Atmos. Sci.*, **64,** 3044-3067.
Yanase, W., G. Fu, H. Niino, and T. Kato, 2004: A polar low over the Japan Sea on 21 January 1997. Part II: A numerical study. *Mon. Wea. Rev.*, **132,** 1552-1574.
Yokota, S., H. Niino, and W. Yanase, 2012: Tropical cyclogenesis due to breakdown of intertropical convergence zone: An idealized numerical experiment. *Sola*, **8,** 103-106.